Journal of Sound and Vibration 417 (2018) 1–18

Contents lists available at ScienceDirect

Journal of Sound and Vibration

journal homepage: www.elsevier.com/locate/jsvi

# Damage assessment in a sandwich panel based on full-field vibration measurements

F. Seguel, V. Meruane*

*Department of Mechanical Engineering, Universidad de Chile, Beauchef 851, Santiago, Chile*

ARTICLE INFO

*Article history:*
Received 28 April 2017
Received in revised form 11 October 2017
Accepted 24 November 2017
Available online 6 December 2017

*Keywords:*
Sandwich structure
Debonding
Honeycomb
Full-field vibration measurement
High-speed digital image correlation

ABSTRACT

Different studies have demonstrated that vibration characteristics are sensitive to debonding in composite structures. Nevertheless, one of the main restrictions of vibration measurements is the number of degrees of freedom that can be acquired simultaneously, which restricts the size of the damage that can be identified. Recent studies have shown that it is possible to use high-speed three-dimensional (3-D) digital image correlation (DIC) techniques for full-field vibration measurements. With this technique, it is possible to take measurements at thousands of points on the surface of a structure with a single snapshot. The present article investigates the application of full-field vibration measurements in the debonding assessment of an aluminium honeycomb sandwich panel. Experimental data from an aluminium honeycomb panel containing different damage scenarios is acquired by a high-speed 3-D DIC system; four methodologies to compute damage indices are evaluated: mode shape curvatures, uniform load surface, modal strain energy and gapped smoothing.



## 1. Introduction

Sandwich structures typically consist of thin face sheets or skins and a lightweight thicker core sandwiched between the skins to obtain a structure with superior bending stiffness. The concept of sandwich structures is common in nature; for example, the branches of a tree or the bones in skeletons are examples of sandwich structures with foam-like core materials. The high stiffness and strength at a minimum weight make sandwich structures attractive for use in applications where weight saving is critical. Consequently, in recent years, the applications of sandwich structures have been rapidly increasing and range from satellites, spacecraft, aircraft, ships, automobiles, rail cars, wind energy systems and bridge construction [1].

Nevertheless, despite their advantages, sandwich structures can experience imperfect bonding or debonding between the skins and core because of manufacturing defects or impact loads. Debonding in a sandwich structure may severely degrade its mechanical properties, which can cause catastrophic failure of the overall structure. Therefore, even though making the structure as light as possible without sacrificing strength is a fundamental requirement in aircraft design, the application of sandwich structures remains limited to secondary (non-critical) components [2].

To improve both safety and functionality of these systems, structural damage assessment methodologies can be implemented. The purpose of these methodologies is to detect and characterize damage at the earliest possible stage and to estimate how much time remains before maintenance is required, the structure fails, or the structure becomes no longer usable.

* Corresponding author.
*E-mail address:* vmeruane@ing.uchile.cl (V. Meruane).

https://doi.org/10.1016/j.jsv.2017.11.048
0022-460X/

Damage assessment has a tremendous potential for safety and/or economic benefits; it reduces maintenance costs and increases structural safety and reliability.

Non-destructive inspection (NDI) techniques are frequently used to detect damage in sandwich structures. Some of the techniques used for in-service inspections are visual, tap testing, mechanical impedance, shearography, ultrasonic and thermography inspections [3–5]. Heida and Platenkamp [5] from the Netherlands Aerospace Centre (NLR) investigated different NDI techniques for in-service evaluation of composite aerospace structures. Commercially available NDI equipment was tested to identify impact, delamination and disbond damage in three composite aerospace structures. The results showed that only ultrasonic inspection was able to detect and quantify disbond damage, but the limitations were its small field of view and the requirement to use a couplant. A similar conclusion was reached by Hsu [4] in a large-scale experiment organized by the Sandia Laboratories to evaluate different NDI techniques for honeycomb sandwich structures; it was found that air-coupled ultrasound was the best technique among those investigated. Nevertheless, regardless of the number of NDI techniques available to inspect sandwich panels, some challenges remain [6]:

- the detection of defects/damage in thick sandwich structures remains limited,
- it is generally not possible to detect far-side defects with one-sided inspection methods,
- during inspections, it may be difficult to distinguish between damage and hidden features of the structure, and
- there is insufficient knowledge about the sensitivity and reliability of NDI when applied to sandwich composites.

In addition, NDI techniques are time-consuming, need prior knowledge of the damage location and require access to the portion of the structure being inspected, which can be impractical in some cases.

### 1.1. Vibration-based damage assessment

A global technique called vibration-based damage assessment has been expanding rapidly in recent years [7]. The basic idea is that vibrational characteristics such as natural frequencies, mode shapes, damping and frequency response functions are functions of the physical properties of a structure. Thus, changes to the material and/or its geometric properties owing to damage will cause detectable changes in its vibrational characteristics.

Different studies have demonstrated that vibrational characteristics are sensitive to debonding in sandwich structures. The first numerical investigation was performed by Jiang et al. [8] who modelled debonded honeycomb structures with a commercial finite element software. Their results showed that natural frequencies are sensitive indicators to the presence of debonding. The finite-element method was also used by Burlayenko et al. [9,10] to study the influence of skin/core debonding on the vibrations of honeycomb panels, concluding that the size of the debonded zone reduces the natural frequencies and creates a discontinuity in the mode shapes. Similar conclusions were found in the experimental and theoretical/numerical investigations of Kim and Hwang [11] and Lou et al. [12], where it was concluded that natural frequencies decrease because of a loss of stiffness caused by local damage and that vibration modes show local deformation in the damaged region. On the other hand, the experimental study performed by Shahdin et al. [13] showed that the damping ratio is a more sensitive parameter for damage detection than the natural frequencies, although it is much harder to estimate. Meruane at al [14,15]. demonstrated that it is possible to identify debonding in honeycomb sandwich panels using the changes in natural frequencies and mode shapes.

Vibration-based damage assessment methods are classified as model-based or non-model based. Model-based methods are particularly useful for predicting system response to new loading conditions and/or new system configurations. Nevertheless, the performance of a model-based damage assessment algorithm relies on the quality of the structure's numerical model. If the numerical model is not accurate, it becomes difficult to distinguish between numerical errors and actual changes owing to damage. On the hand, non-model-based methods detect damage by comparing the measurements from the damaged and undamaged structures with no need of a numerical model.

Many response parameters have been used in non-model damage assessment and include natural frequencies [16], spatial correlation of mode shapes [17], mode shape curvatures [18], modal flexibility and its derivatives [19,20] and modal strain energy (MSE) [21]. Most have been developed for one-dimensional (1-D) structures such as beams, frames, and truss structures, while only a few studies have investigated damage assessment of two-dimensional (2-D) (plate-like) structures. Cornwell et al. [22] were the first to use strain energy in a damage localization method for plate-like structures. The damage index was computed using the strain energy of a plate in the damaged and undamaged states. The method was validated using numerical simulations and with experimental data of an aluminium plate with saw cuts. Lin et al. [23] investigated the identification of damage in plate-like structures using a strain mode technique derived from the Rayleigh–Ritz approach. The authors proposed two damage indices, the bending moment index and the residual strain mode shape index. Their results showed that the bending moment is more sensitive than the strain mode shape, but the detection depends on the damage location, whereas the residual strain mode shape detects damage accurately independent of the location. Wu and Law [24] developed a damage localization method for plate structures based on changes in the uniform load-surface (ULS) curvature. ULS is defined as the deflection vector of a structure under a uniform load. The method was validated with numerical data of different plates, and damage was introduced as a localized stiffness reduction. In a later work, Wu and Law [25] proposed a model-based damage assessment algorithm that also used changes in the ULS curvature. The inverse problem was modelled

as a linear equation system based on a first-order Taylor series approximation and solved iteratively. Yoon et al. [26] presented a baseline-free damage localization algorithm for plate-like structures. The algorithm used vibration mode curvatures and a 2-D gapped smoothing (GS) method to locate changes in structural stiffness. The condition to locate damage without baseline data was that the structure was homogeneous with respect to stiffness in the undamaged case. Qiao et al. [27] studied the experimental identification of delamination in a composite laminate plate using three different methodologies: GS, generalized fractal dimension, and modal strain energy (MSE). Experimental data were measured by two approaches: scanning laser vibrometer (SLV) and polyvinylidene fluoride (PVDF) sensor. The results show that an SLV provides better results than a PVDF sensor because of its refined scanning mesh. However, although all the three methods can detect the actual location of damage, they also show extra peaks at other locations (false damage). The authors concluded that the GS method identifies the delamination of composite plates better than other algorithms. Moreno–García et al. [28] investigated the use of higher-order mode shape derivatives to locate damage in plate-like structures. The authors concluded that a damage indicator based on the fourth-order spatial derivative allows better damage localization. In addition, as the number of measured degrees of freedom (DOFs) increases, the success in damage localization also increases.

### 1.2. Full-field vibration measurements

One of the main restrictions of vibration measurement is the number of DOFs that can be acquired simultaneously. Over the last decades, there has been tremendous progress in finite element modelling; the DOF of these models has grown to over a million in many applications, whereas the number of measurement points has been limited to the order of hundreds. This large mismatch between experimental and numerical DOF has led to the search for full-field vibration-measurement techniques.

Common techniques to obtain full-field vibration measurements include the use of a wide array of triaxial accelerometers or an SLV. The use of accelerometers can mass-load a structure, and the number of measurement points is limited by the number of accelerometers available. On the other hand, an SLV can provide three-dimensional (3-D) data at many points but can only make measurements asynchronously. In addition, the performance of a vibrometer is affected by the presence of large rigid-body motion. Recent studies have shown it is possible to use high-speed 3-D digital image correlation (DIC) techniques for full-field vibration measurements. The DIC technique uses images taken from a pair of stereo cameras to determine the 3-D geometry and displacements of an object whose surface contains a speckle pattern. With this technique, it is possible to take measurements at thousands of points on the surface of a structure with a single snapshot.

Helfrick et al. [29] were the first to investigate high-speed 3-D DIC technique for full-field vibration measurements. The authors compared the mode shapes obtained by an SLV, accelerometers and DIC and concluded that DIC has tremendous potential for full-field vibration-measurement applications. Table 1 compares the three methods. The principal advantages of DIC are high spatial resolution, absence of contact and mass loading and low sensitivity to rigid-body motion.

Wang et al. [30] presented a model-updating method that used full-field vibration measurements acquired with a DIC system. The discrepancies between numerical and experimental mode shapes were assessed by using shape-feature vectors constructed from Tchebichef moment descriptors. In a later work, Wang et al. [31] computed the frequency-response functions (FRF) of shape features from DIC measurements. An advantage of this approach is that mode shapes identified from FRF of shape features have no measurement noise. Trebuňa and Hagara [32] presented a method to perform operational and experimental modal analysis from experimental data obtained with a high-speed DIC system. According to the authors, the main advantage of this system was that it was possible to obtain multiple FRFs in one measurement, thus the duration of the experiment was remarkably small. Ha et al. [33] showed that a high-speed DIC system can be used to perform a modal analysis of an artificial wing mimicking a beetle's hind wing. Given the size and light weight of this structure, it was not possible to perform a modal analysis with conventional accelerometers.

**Table 1**
Comparison between accelerometer, DIC and SLV for modal analysis [29].

| Accelerometer | DIC | SLV |
|---|---|---|
| 1. Easy to obtain transfer functions | 1 Obtaining transfer functions requires post-processing beyond typical software capabilities | 1. Easy to obtain transfer functions |
| 2. Data only at locations of response transducers | 2 Data on entire visible surface of an object | 2. Data at predefined points on visible surface of an object |
| 3. Sensitivity depends on accelerometer | 3 Sensitivity decreases as the field of view increases | 3. Sensitivity related to laser light wavelength |
| 4. Broadband excitation of all modes | 4 Better suited for single-frequency excitation | 4. Broadband excitation of all modes |
| 5. No stability requirements | 5 Less sensitive to camera rigid-body motion | 5. Calibration highly sensitive to changes in setup conditions |
| 6. Inexpensive | 6 Expensive | 6. Very expensive |
| 7. Require contact and possible mass loading | 7 Non-contacting and non-mass loading | 7. Non-contacting and non-mass loading |
| 8. Low spatial resolution | 8 Very high spatial resolution | 8. High spatial resolution |

The large potential of full-field vibration measurements acquired with high-speed 3-D DIC systems has not yet been explored for structural damage assessment. Some of the advantages over current methods are:

- Measuring vibrations over the full surface of an object provides much useful information and allows the detection of small changes that are undetectable with conventional methods. Therefore, smaller damage can be detected.
- A higher spatial resolution allows for computing displacement derivatives with more precision. These derivatives have been shown to be useful damage indicators; thus, a higher spatial resolution will allow damage assessment with more precision.
- A high-speed 3-D DIC is a non-contacting system that does not mass-load a structure. Therefore, unlike accelerometers, the properties of a structure are not altered by the measurement system.

Nevertheless, despite its advantages, DIC measurements have a lower sensitivity than accelerometers or laser measurements and a lower frequency range. Therefore, it is of interest to investigate whether the advantages outweigh the disadvantages and if this method can be used effectively for damage identification. The present article investigates the application of full-field vibration measurements in the debonding assessment of an aluminium honeycomb sandwich panel. First, the performance of four methodologies to compute damage indices were evaluated using simulated numerical data. The methodologies were mode shape curvatures, ULS, MSE and GS. Then, experimental data from an aluminium honeycomb panel containing different damage scenarios were acquired by a high-speed 3-D DIC system and the four methodologies were evaluated on the basis of this data.

## 2. Damage index

### 2.1. Mode shape curvatures

In the absence of damage, mode shapes have a known smooth surface; whereas in the presence of damage, sharp changes such as an abrupt slope might appear at a damage location. Since there is a clear change in the mode shape curvature in the vicinity of damage, a change in curvature has been adopted to locate damage.

For 1-D structures, the curvature of the $r$-th mode shape at the $i$-th test point can be obtained with the central difference approximation

$$\frac{\partial^2 \phi_r(x_i)}{\partial x^2} = \left(\phi_r(x_{i+1}) + \phi_r(x_{i-1}) - 2\phi_r(x_i)\right) \Big/ h^2, \tag{1}$$

where $\phi_r(x_i)$ is the $r$-th mode shape at the $i$-th test point and $h$ is the uniform separation of the test grid. The damage index is obtained by calculating the absolute difference between the curvatures of the damaged and undamaged cases as [18].

$$d_r(x_i) = \left| \frac{\partial^2 \phi_r^D(x_i)}{\partial x^2} - \frac{\partial^2 \phi_r^U(x_i)}{\partial x^2} \right|. \tag{2}$$

The superscripts D and U refer to damaged and undamaged, respectively.

In the case of 2-D structures, the curvature at point $(x_i, y_j)$ in each normal direction along the sensor grid is calculated as

$$\frac{\partial^2 \phi_r\left(x_i, y_j\right)}{\partial x^2} = \frac{\phi_r\left(x_{i+1}, y_j\right) - 2\phi_r\left(x_i, y_j\right) + \phi_r\left(x_{i-1}, y_j\right)}{h_x^2} \tag{3}$$

$$\frac{\partial^2 \phi_r\left(x_i, y_j\right)}{\partial y^2} = \frac{\phi_r\left(x_i, y_{j+1}\right) - 2\phi_r\left(x_i, y_j\right) + \phi_r\left(x_i, y_{j-1}\right)}{h_y^2} \tag{4}$$

where $h_x$ and $h_y$ are the uniform grid spacing in the corresponding directions. The damage index can be formulated as

$$d_r\left(x_i, y_j\right) = \left( \left| \frac{\partial^2 \phi_r^D\left(x_i, y_j\right)}{\partial x^2} - \frac{\partial^2 \phi_r^U\left(x_i, y_j\right)}{\partial x^2} \right| + \left| \frac{\partial^2 \phi_r^D\left(x_i, y_j\right)}{\partial y^2} - \frac{\partial^2 \phi_r^U\left(x_i, y_j\right)}{\partial y^2} \right| \right)^2. \tag{5}$$

Considering $m$ modes, the damage index at test point $(x_i, y_j)$ is computed as

$$d\left(x_i, y_j\right) = \sum_{r=1}^{m} d_r\left(x_i, y_j\right). \tag{6}$$

### 2.2. Uniform load surface

The flexibility matrix is basically defined as the inverse of the stiffness matrix, which can be written in modal form as

$$G = \mathbf{\Phi}\mathbf{\Lambda}^{-1}\mathbf{\Phi}^T = \sum_r \frac{\phi_r \phi_r^T}{\omega_r^2}, \tag{7}$$

where $\mathbf{\Phi}$ and $\mathbf{\Lambda}$ are the eigenvector and eigenvalue matrices, respectively, $\phi_r$ and $\omega_r$ are the $r$-th mode shape and natural frequency, respectively, and $(.)^T$ indicates the vector transpose. From Equation (7) we can see that the higher the frequency, the smaller the modal contribution to the flexibility matrix. According to Jaishi et al. [34], a good estimation of the flexibility matrix may be obtained from only a few low-frequency modes at a reduced set of measured DOF.

The modal deflection at point $k$ under unit load at point $l$ is given by

$$G_{k,l} = \sum_{r=1}^{m} \frac{\phi_r(k)\phi_r(l)}{\omega_r^2}, \tag{8}$$

were $m$ is the number of available modes. The ULS at a point $k$ is defined as the modal deflection at this point under uniform load over the entire structure and can be approximated as

$$ULS(k) = \sum_{r=1}^{m} \frac{\phi_r(k)\sum_{l=1}^{n}\phi_r(l)}{\omega_r^2}, \tag{9}$$

where $n$ is the number of DOFs. The ULS is expected to reduce the effect of the experimental noise because the summation of the modal coefficients averages out the random error at each point [25].

As in the case of mode shape displacements, the ULS curvature is a more sensitive indicator of damage. Therefore, the damage index can be formulated as [24].

$$\delta(k) = \left( \left| \frac{\partial^2 ULS^D(k)}{\partial x^2} - \frac{\partial^2 ULS^U(k)}{\partial x^2} \right| + \left| \frac{\partial^2 ULS^D(k)}{\partial y^2} - \frac{\partial^2 ULS^U(k)}{\partial y^2} \right| \right)^2. \tag{10}$$

### 2.3. Modal strain energy

The MSE is a sensitive indicator of damage and has frequently been used to locate damage in 1-D structures such as beams, frames and trusses [21]. Cornwell et al. [22] introduced the strain energy damage detection method for plate-like structures. The damage indices are computed using the MSE of a plate in the damaged and undamaged states. In the case of a plate-like structure, for a particular mode shape, $\phi_r$, the strain energy associated with that mode shape is

$$U_r = \frac{D}{2}\int_0^b \int_0^a \left(\frac{\partial^2\phi_r}{\partial x^2}\right)^2 + \left(\frac{\partial^2\phi_r}{\partial y^2}\right)^2 + 2\nu\left(\frac{\partial^2\phi_r}{\partial x^2}\right)\left(\frac{\partial^2\phi_r}{\partial y^2}\right) + 2(1-\nu)\left(\frac{\partial^2\phi_r}{\partial x \partial y}\right)^2 dxdy, \tag{11}$$

where $a$ and $b$ are the plate dimensions and $D = Eh^3/12(1-\nu^2)$ is the bending stiffness of the plate. By dividing the plate into sub-regions, it is possible to locate damage by comparing the normalized strain energy of each sub-region in the damaged and undamaged conditions. The energy associated with sub-region $jk$ for the $r$-th mode shape is given by

$$U_{r,jk} = \frac{D_{jk}}{2}\int_{b_k}^{b_{k+1}} \int_{a_j}^{a_{j+1}} \left(\frac{\partial^2\phi_r}{\partial x^2}\right)^2 + \left(\frac{\partial^2\phi_r}{\partial y^2}\right)^2 + 2\nu\left(\frac{\partial^2\phi_r}{\partial x^2}\right)\left(\frac{\partial^2\phi_r}{\partial y^2}\right) + 2(1-\nu)\left(\frac{\partial^2\phi_r}{\partial x \partial y}\right)^2 dxdy; \tag{12}$$

therefore,

$$U_r = \sum_{k=1}^{N_x}\sum_{j=1}^{N_y} U_{r,jk}, \tag{13}$$

where $N_x$ and $N_y$ are the number of divisions in the $x$ and $y$ directions, respectively. The fractional energy at location $jk$ is

$$F_{r,jk=}\frac{U_{r,jk}}{U_r}. \tag{14}$$

The same procedure can be used to compute the fractional energy at location $jk$ for the $r$-th mode of the damaged structure $F^D_{r,jk}$. To account for all measured modes, the damage index for sub-region $jk$ is defined as

$$\beta_{jk} = \sum_{i=1}^{m} F^D_{r,jk} \Big/ \sum_{i=1}^{m} F_{r,jk}, \tag{15}$$

where $m$ is the number of measured modes. Assuming that the collection of damage indices represents a population of a normally distributed random variable, a normalized damage index is obtained using

$$Z_{jk} = \left(\beta_{jk} - \overline{\beta}_{jk}\right) \Big/ \sigma_{jk}, \tag{16}$$

where $\overline{\beta}_{jk}$ and $\sigma_{jk}$ represent the mean and standard deviation of the damage indices, respectively.

### 2.4. Gapped smoothing method

The 2-D GS method developed by Yoon et al. [26] starts by normalizing the operational deflection shape by its root mean square values,

$$\varphi_r\left(x_i, y_j\right) = \phi_r\left(x_i, y_j\right) \sqrt{\frac{N_x N_y}{\sum_{i=1}^{N_x}\sum_{j=1}^{N_y} \phi_r^2\left(x_i, y_j\right)}}, \tag{17}$$

where $N_x$ and $N_y$ are the number of grid points in the $x$ and $y$ directions, respectively, and $\varphi_r(x_i, y_j)$ is the normalized $r$-th mode shape at point $(x_i, y_j)$.

The mode shape curvatures are estimated by the central difference approximation as

$$\nabla^2\varphi_r\left(x_i, y_j\right) = \frac{\varphi_r\left(x_{i+1}, y_j\right) - 2\varphi_r\left(x_i, y_j\right) + \varphi_r\left(x_{i-1}, y_j\right)}{h_x^2} + \frac{\varphi_r\left(x_i, y_{j+1}\right) - 2\varphi_r\left(x_i, y_j\right) + \varphi_r\left(x_i, y_{j-1}\right)}{h_y^2}, \tag{18}$$

where $h_x$ and $h_y$ represent the uniform grid spacing in the corresponding directions. Then, the mode shape curvatures are expressed as

$$\nabla^2\varphi_r\left(x_i, y_j\right) = g_{i,j}^T \theta_{i,j}, \tag{19}$$

where $g_{i,j}$ is a base function vector that depends on the grid point locations and $\theta_{i,j}$ is a vector of parameters. In Ref. [26] the base function and parameter vectors were constructed as

$$g_{i,j}^T = \left[1, x_i, y_j\right], \quad \boldsymbol{\theta}_{i,j}^T = \left[a_0, a_1, a_2\right]. \tag{20}$$

Considering the points around $(x_i, y_j)$, Equation (19) can be expressed as

$$\boldsymbol{\lambda}_r\left(x_i, y_j\right) = \mathbf{G}_r^T\left(x_i, y_j\right)\theta_{i,j}, \tag{21}$$

where

$$\boldsymbol{\lambda}_r^T\left(x_i, y_j\right) = \left[\nabla^2\varphi_r\left(x_{i-1}, y_{j-1}\right), \nabla^2\varphi_r\left(x_i, y_{j-1}\right), \nabla^2\varphi_r\left(x_{i+1}, y_{j-1}\right), \cdots, \nabla^2\varphi_r\left(x_{i+1}, y_{j+1}\right)\right]$$

$$\mathbf{G}_r^T\left(x_i, y_j\right) = \left[\mathbf{g}_{i-1,j-1}, \mathbf{g}_{i,j-1}, \mathbf{g}_{i+1,j-1}, \cdots, \mathbf{g}_{i+1,j+1}\right].$$

The least square estimation of the parameters is given by

$$\widehat{\boldsymbol{\theta}}_{\boldsymbol{i,j}}^{\mathbf{r}} = \left(\mathbf{G}_r^T\left(x_i, y_j\right)\mathbf{G}_r\left(x_i, y_j\right)\right)^{-1}\mathbf{G}_r^T\left(x_i, y_j\right)\lambda_r\left(x_i, y_j\right). \tag{22}$$

The smoothed mode shape curvature is computed using the estimated parameters

$$C_r\left(x_i, y_j\right) = g_{ij}^T \widehat{\boldsymbol{\theta}}_{\boldsymbol{ij}}^{\boldsymbol{r}}, \tag{23}$$

and the damage indices are calculated as

$$d_r\left(x_i, y_j\right) = \left|\nabla^2 \varphi_r\left(x_i, y_j\right) - C_r\left(x_i, y_j\right)\right|. \tag{24}$$

Finally, considering $m$ modes, the damage index at test point $(x_i, y_j)$ is computed as

$$d\left(x_i, y_j\right) = \sum_{r=1}^{m} d_r\left(x_i, y_j\right). \tag{25}$$

## 3. Statistical treatment

In most of the undamaged regions in the panels, the damage indices are greater than zero. To discriminate between real damage and false damage, statistical treatment of the data can be performed [26]. The basic idea is that the mean and standard deviation of averaged damage indices in the undamaged regions of the damaged panels are similar. Assuming a normal distribution, the outliers will be damage indices coincident with statistically significant features such as local damage.

The present study adopted the Grubbs' test to construct the damage map, the procedure is as follows [35]:

1. First, let $\delta_k$ represent the damage index at point k, the maximum normed residual (MNR) is defined as

$$MNR = \max_k \left|\frac{\delta_k - \overline{\delta}}{\sigma}\right|, \tag{26}$$

where $k = 1, 2, \ldots, n$, $n$ is the total number of grid points and $\overline{\delta}$ and $\sigma$ are the mean and standard deviation of the damage indices, respectively.

2. The MNR is compared with the critical value (CV) for the sample size $n$:

$$CV = \frac{t(n-1)}{\sqrt{n\left(n-2+t^2\right)}}, \tag{27}$$

where $t$ is the $1 - \alpha/2n$ quantile of the Student's $t$ distribution with an $n$-2 DOF and a 5% significance level.

3. If the MNR is larger than the CV, the point associated with the MNR is declared an outlier and is removed from the original data. Steps 1 to 3 are repeated until the MNR becomes smaller than the CV.
4. All the points identified as outliers are declared as damaged and included in the damage map; the remaining points have their indices set to zero. Therefore, the damage map consists only of outliers from the statistical treatment.

## 4. Noise reduction

The damage indices described in the previous section require the computation of second-order derivatives. These derivatives can be computed by applying a central finite difference formulation. However, since this formulation leads to the propagation and amplification of measurement errors and noise which is always present in experimental data, it is important to implement noise reduction or smoothing techniques to reduce experimental noise without affecting the detection of damage. In general, data smoothing can be performed by parametric or nonparametric regression. Unlike nonparametric regression, parametric regression requires prior knowledge of analytical functions that can represent the data. Examples of parametric functions used to smooth displacement measurements are radial basis functions [36] and finite element shape functions [37,38], whereas the most common nonparametric approaches are based on least squares [39,40].

Let us consider the following 1-D noisy data:

$$y = \widehat{y} + \varepsilon, \tag{28}$$

where $\widehat{y}$ is the actual data and $\varepsilon$ represents noise. Smoothing methodologies try to obtain the best estimate of $\widehat{y}$. Parametric methods require a regression equation that represents the data. If an analytical regression equation is not available, then, nonparametric regression is the best option. Some nonparametric regression methods described in literature are kernel regression, local polynomial regression, Savitzky–Golay filter and penalized least squares regression. The penalized least squares regression technique consists of a minimizing criterion that balances the fidelity of the data measured by the residual sum of squares and a penalty term that reflects the roughness of the smooth data, which can be selected as a second-order divided difference [40]:

$$F(\widehat{y}) = \|y - \widehat{y}\|^2 + \|D\widehat{y}\|^2, \tag{29}$$

where D is a tridiagonal square matrix. Solving the minimization problem yields

$$\left(I_n + sD^T D\right)\widehat{y} = y \tag{30}$$

In the case of evenly spaced data, relatively fast algorithms based on Cholesky decomposition [41] or discrete cosine transform [40] can be used to solve (30).

Here the smoothing technique proposed by Garcia [40] was implemented to reduce the experimental noise in mode shapes. This is a fully automated smoothing procedure for uniformly sampled gridded data. The algorithm is based on the penalized least square method by means of the discrete cosine transform. In addition, this method allows for the completion of missing information, which is a common problem with vibration mode shapes identified from DIC measurements. Sometimes, because of bad lighting or poor focus, displacements in parts of a structure are not captured.

## 5. Application case

### 5.1. Experimental measurements

The experimental structure consisted of a sandwich panel of 0.25 m × 0.35 m x 0.021 m made of an aluminium honeycomb core bonded to two aluminium skins. The skins were bonded to the honeycomb core using an epoxy adhesive. Fig. 1(a) shows the aluminium sheet with a layer of epoxy adhesive; the circular region without adhesive, that can be seen in the figure, was introduced to simulate debonding. To ensure perfect bonding, the panel was cured using a vacuum bagging system as shown in Fig. 1(b).

Fig. 2 shows the experimental setup. The panel was attached to an electrodynamic shaker driven by a function generator and signal amplifier. The panel displacements were captured by two high-speed synchronized cameras connected to DIC software. The cameras, data acquisition and DIC software corresponded to the Q450 high-speed DIC system of Dantec Dynamics. The cameras had a maximum acquisition frequency of 7530 FPS at a resolution of 1 MP.

The following procedure was performed to identify the experimental vibration mode shapes.

- First, the panel was excited at different points by an impact hammer, and the response was captured by a miniature accelerometer. The experimental data was processed to obtain the Frequency Response Functions (FRFs) from which the natural frequencies were identified by peak-picking.
- A speckle pattern was added to the panel by means of an adhesive sheet. The pattern provided by Dantec Dynamics had been optimized for DIC measurements. The cameras were calibrated, and the image correlation parameters were selected to minimize experimental error by following the recommendations of Siebert et al. [42].
- In the case of high-speed DIC measurements, single-frequency excitation has been shown to be the best method for identifying experimental mode shapes [29,43]. Therefore, to identify mode shapes, the shaker excited the panel with a sinusoidal vibration tuned to the natural frequency to cause the panel to vibrate in resonance. Images were captured at a rate of 5 kHz with a resolution of 1024 × 1024 pixels. The number of mode shapes that could be identified varied from five to seven depending on the panel. Fig. 3 shows the vibration measurements with the high-speed DIC system and a vibration mode shape at 444 Hz.
- The experimental displacements were exported as hdf5 files and imported into MATLAB. The Fourier transform of the displacements was computed, and then the amplitude and phase at the resonance frequency was recorded at each point. With this information, the operational mode shape at the resonant frequency was reconstructed.
- Finally, the smoothing technique proposed by Garcia [21] was applied to reduce the experimental noise and to complete the missing information in the mode shapes.

Figs. 4 and 5 present the first six experimental model shapes for a damaged and an undamaged panel. In both cases, it was possible to see the effect of the shaker attachment in the middle of the panel. As expected, most of the natural frequencies of

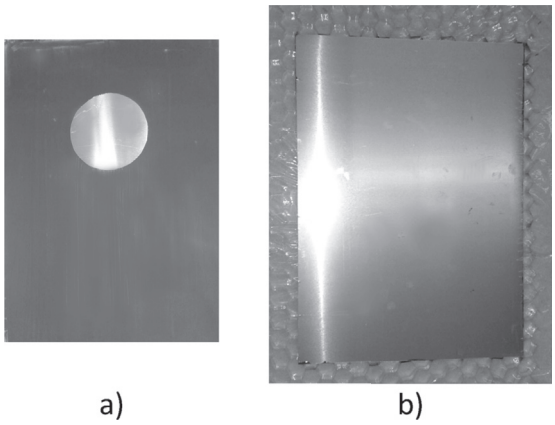


**Fig. 1.** Fabrication of experimental panel: a) layer of epoxy adhesive over skin and b) vacuum bagging of panel.

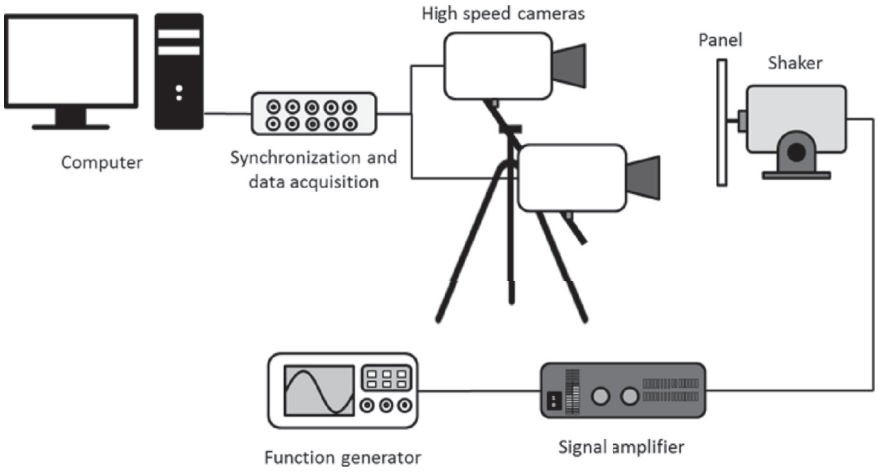


**Fig. 2.** Experimental setup.

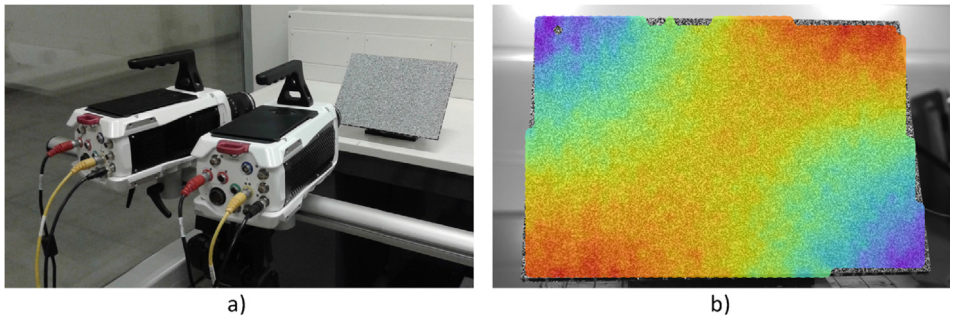


**Fig. 3.** Vibration measurements acquired with high-speed 3-D DIC System: a) high-speed cameras aimed at panel and b) vibration mode shape at 444 Hz.

the damaged panel were lower than those of the undamaged case. The largest differences in mode shapes were found in the modes with higher frequencies.

### *5.2. Numerical model*

A first evaluation of the performance of three damage assessment algorithms was performed using a numerical model of the panel. The numerical model was developed and validated in Ref. [14]. The honeycomb panel was modelled with finite

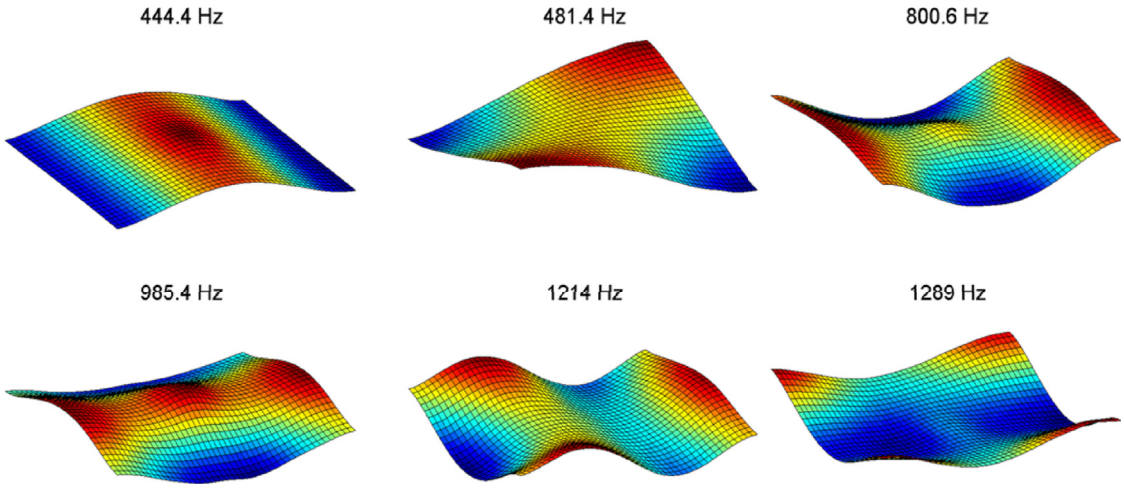


**Fig. 4.** Identified mode shapes for undamaged case.

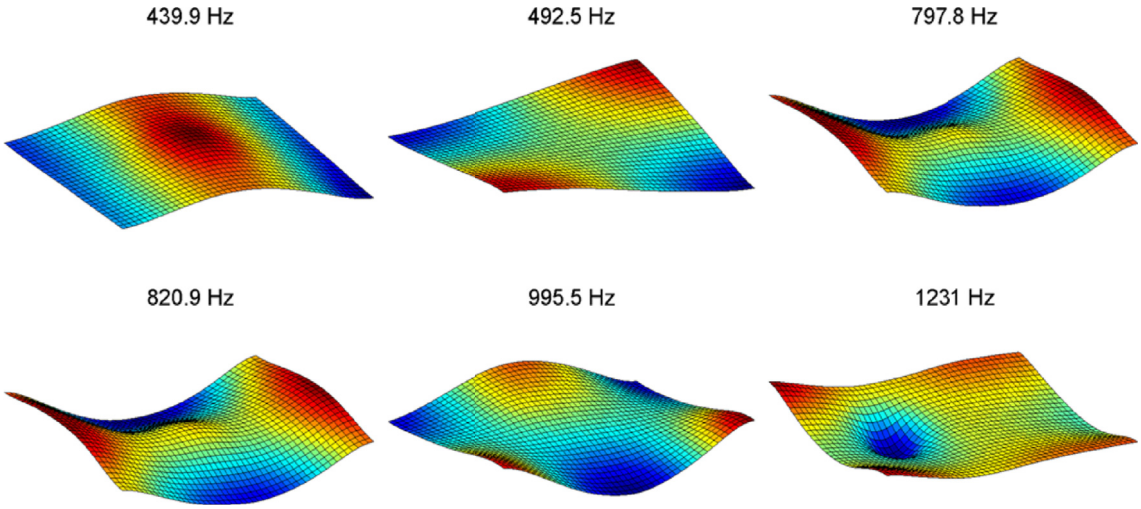


**Fig. 5.** Identified mode shapes for debonded case.

elements using a simplified three-layer shell model. The adhesive layer between the skin and core was modelled using linear springs with reduced rigidity in the debonded sectors as shown in Fig. 6.

The numerical model was built in MATLAB® using the Structural Dynamics Toolbox (SDT) [44]. The skins and honeycomb panel were modelled with standard isotropic four-node shell elements. The final model had 10,742 shell and 7242 spring elements.

The mechanical properties of the sandwich construction depended upon the adhesives, temperature and pressure used during curing. In addition, the anisotropic nature of the honeycomb core made testing of the sandwich specimen mandatory to accurately determine their properties. In Ref. [14], the mechanical properties of the adhesive layer and the honeycomb core were determined by updating the finite element model with the experimental mode shapes and natural frequencies for both the damaged and undamaged cases.

To simulate the experimental measurements, the numerical modes were first contaminated with 5% random noise and then smoothed using the noise reduction technique presented in Section 4.

## 6. Results

Computation of the damage indices was necessary to define pairs of damaged and undamaged mode shapes. The modal assurance criterion (MAC) was used for this calculation. MAC is defined by Allemang and Brown [45] as

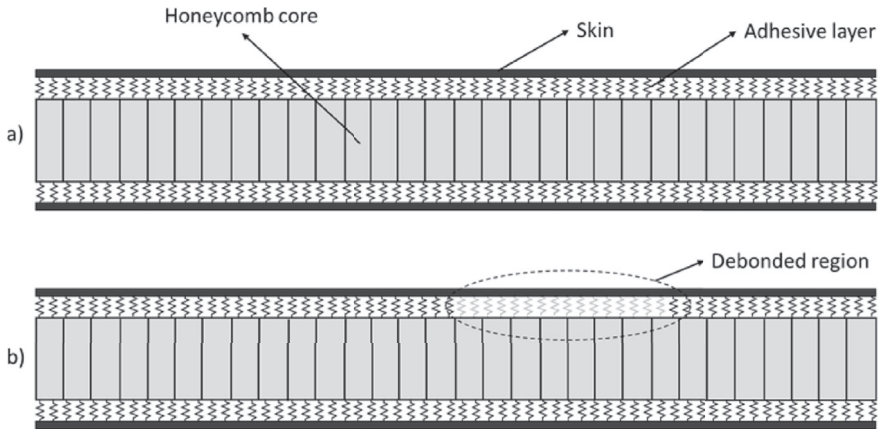


**Fig. 6.** Lateral view of numerical model: a) undamaged panel and b) panel with a debonded region.

$$MAC_{r,i} = \frac{\left(\phi_r^{D^T}\phi_i^U\right)^2}{\left(\phi_r^{D^T}\phi_r^D\right)\left(\phi_i^{U^T}\phi_i^U\right)}, \tag{31}$$

where $\phi_r^D$ $r$-th is the damaged mode shape and $\phi_i^U$ is the $i$-th undamaged mode shape. MAC is a factor that expresses the correlation between two modes. A value of 0 indicates no correlation, whereas a value of 1 indicates two completely correlated modes. Here, the criterion used to define a pair of modes was a MAC value higher than 0.6 and a frequency difference lower than 30%.

In addition to pairing the mode shapes, it was also important that the mode-shape pairs have the same normalization. Nevertheless, operational mode shapes have arbitrary normalization, thus the scaling of the mode-shape pairs will be inconsistent. To handle this, the damaged mode shape may be scaled to the undamaged mode shape by multiplying it by the modal scale factor (MSF),

$$\phi_r^{D^*} = \phi_r^D * MSF_r, \tag{32}$$

$$MSF_r = \frac{\phi_r^{U^T}\phi_r^D}{\phi_r^{D^T}\phi_r^D}, \tag{33}$$

where $\phi_r^{D^*}$ is the scaled damaged mode shape and $MSF_r$ is the modal scale factor for the $r$-th mode-shape pair. Multiplying the experimental mode shape by the corresponding MSF also solves the problem of both mode shapes being out of phase by 180°.

After pairing and scaling the mode shapes, the damage indices were computed following the procedures described in Section 2. In the case of the GS method, there was no need to pair or scale the mode shapes since the algorithm uses only damaged modes (with no baseline).

To evaluate the performance of the algorithms, the elements in the debonded skin were classified using the confusion matrix of Table 2.

From this matrix, the following performance indicators are defined as

$$\begin{aligned} \textit{False Positive Rate } (FPR) &= \frac{FP}{FP+TN} \\ \textit{False Negative Rate } (FNR) &= \frac{FN}{TP+FN} \end{aligned} \tag{34}$$

**Table 2**
Confusion matrix.

| | Total population | True condition | |
|---|---|---|---|
| | | Damage | Undamaged |
| Predicted condition | Damage | True positive (TP) | False positive (FP) |
| | Undamaged | False negative (FN) | True negative (TN) |

The FPR is the ratio of undamaged elements that were wrongly classified as damaged, and the FNR is the ratio of damaged elements that were wrongly classified as undamaged.

### 6.1. Numerical results

A database with one thousand panels under different damage scenarios was built using the numerical model. The panels had circular debonded regions located randomly through the panel with randomly defined diameters between 1 cm and 10 cm.

The performance of the algorithms was evaluated as a function of damage size, measured skin and number of modes. The results are presented in the next sections.

#### 6.1.1. Damage size

The panels in the database were classified into nine groups according to their size, and the performance indicators FPR and FNR were computed for each group. In the case of the mode shape curvature, ULS and MSE methodologies, the first six mode-shape pairs were used, whereas the GS method was implemented with all the damaged modes in the same frequency range as the mode-shape pairs. Therefore, the GS method may include damaged modes that could not be paired with undamaged modes. The results are illustrated in Fig. 7.

For damage with sizes greater than 4 cm, the MSE provided the lowest FNR and detected most of the actual damage. The GS method provided the lowest FNR for damages smaller than 4 cm and was the only algorithm that could detect damages in the range 1–2 cm. The FPR was small for all algorithms and its magnitude had an inverse relationship with the FNR (i.e. when the FPR increased, the FPR decreased).

Figs. 8–11 present examples of the damage identified by the three algorithms for three damage sizes: 3 cm, 5 cm, and 10 cm. Most of the damage was detected by the four algorithms. Nevertheless, the ULS algorithm failed to detect cases of smaller damage and the GS method failed to detect cases of larger damage.

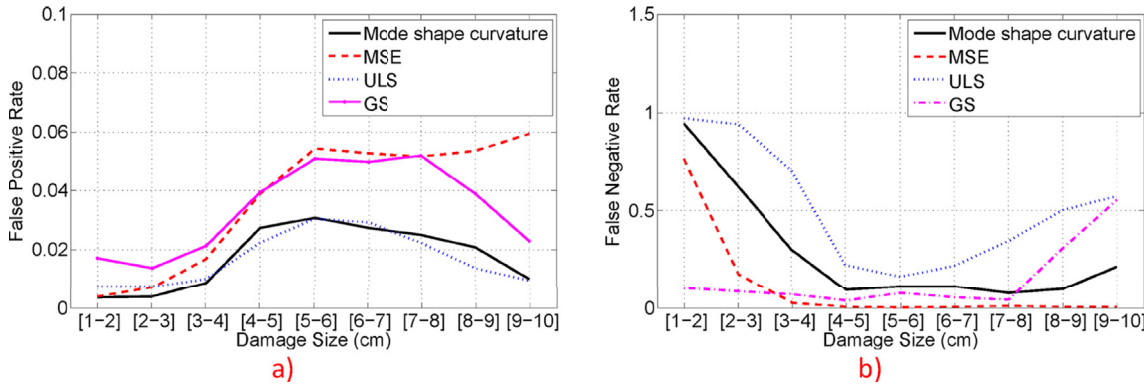


**Fig. 7.** Performance of damage assessment algorithms as a function of damage size: a) FPR and b) FNR.

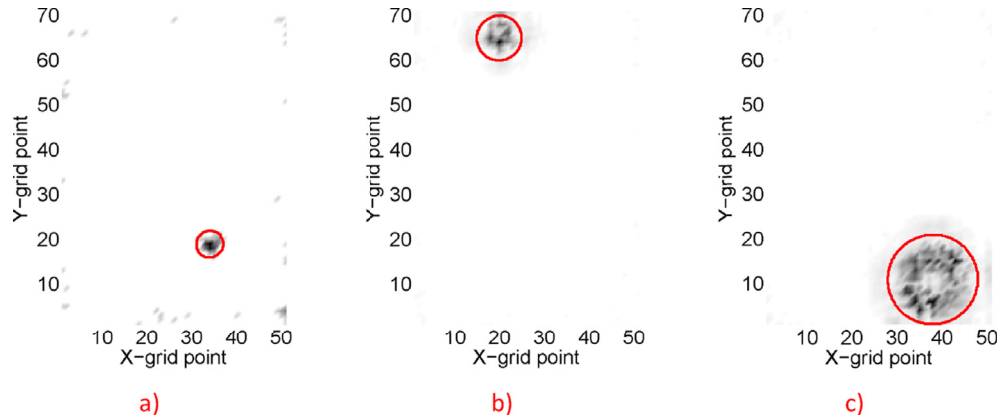


**Fig. 8.** Damage identified by mode shape curvature algorithm. Damage size: a) 3 cm, b) 5 cm and c) 10 cm.

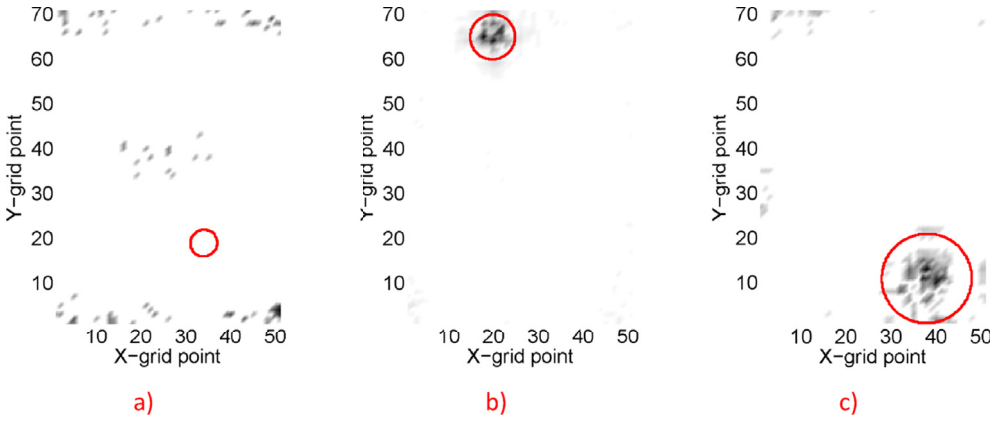


**Fig. 9.** Damage identified by ULS algorithm. Damage size: a) 3 cm, b) 5 cm and c) 10 cm.

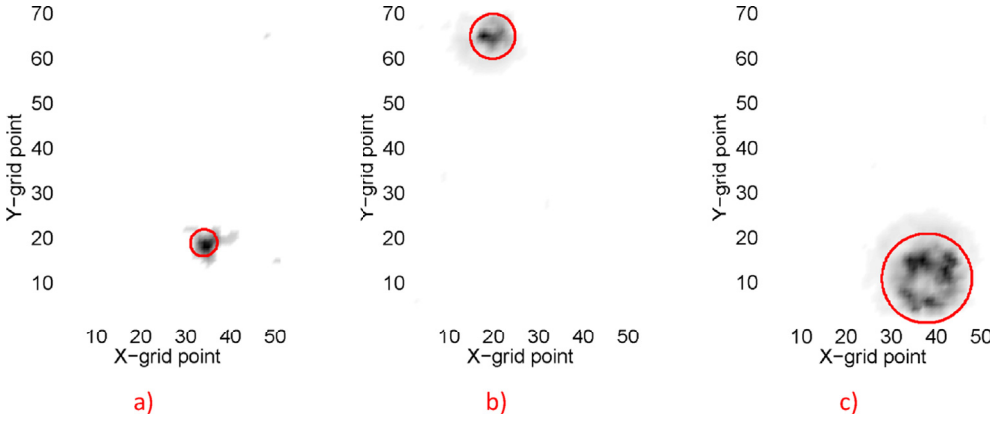


**Fig. 10.** Damage identified by MSE algorithm. Damage size: a) 3 cm, b) 5 cm and c) 10 cm.

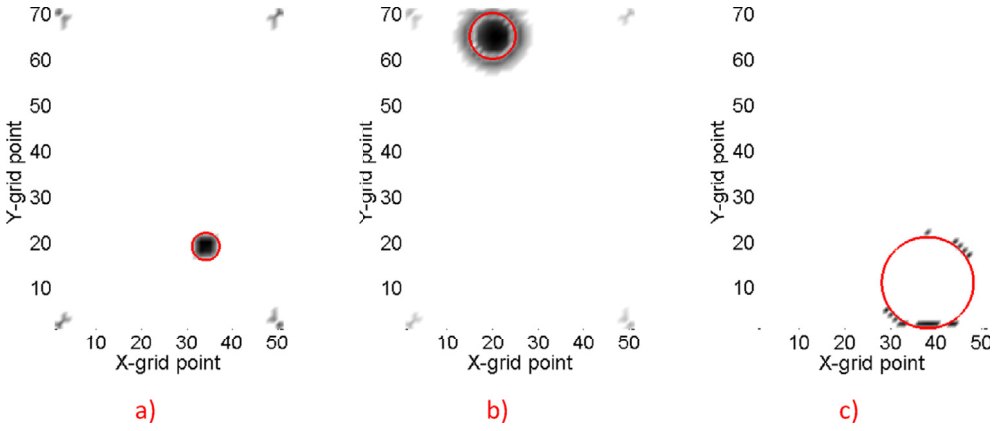


**Fig. 11.** Damage identified by GSM algorithm. Damage size: a) 3 cm, b) 5 cm and c) 10 cm.

### *6.1.2. Measured skin*

The algorithms were evaluated when the vibrations were measured on the skin opposite to the damage. The results are presented in Fig. 12. From the FNR and FPR, it follows that the algorithms barely detected any damage (actual or false) and that no algorithm was able to identify the actual damage. Therefore, in this case, damage can be detected by a shift in the natural frequencies but cannot be localized or quantified.

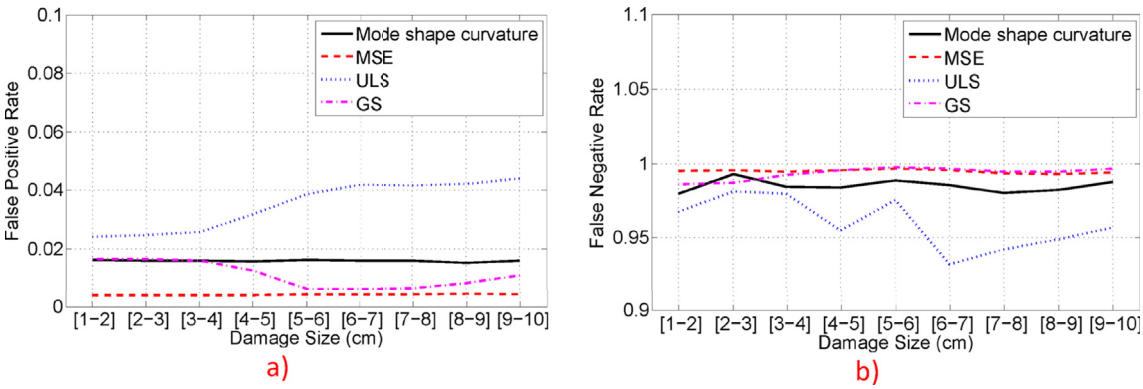


**Fig. 12.** Performance of damage assessment algorithms when vibrations are measured on skin opposite to damage: a) FPR and b) FNR.

### 6.1.3. *Number of modes*

The last analysis pertains to the number of modes. The mode shape curvature, MSE and ULS methodologies were evaluated with different numbers of mode-shape pairs from 1 to 6, whereas the GS method was evaluated using all the damaged modes in the same frequency range as the mode-shape pairs. The results are presented in Fig. 13. All the algorithms showed a decrease in the FNR with an increase in the number of modes, which means that more actual damage was detected with an increase in the number of modes. For up to four modes, the GS method provided a small FNR, while for five to six modes, the MSE provided a slightly smaller FNR. As noted previously, behaviours of the FPR and FNR are inversely related.

## 6.2. *Experimental results*

The algorithm was tested for the three damage scenarios shown in Fig. 14. The first scenario contained a square debonded region, the second had a circular debonded region and the last contained two square debonded regions. To assess the experimental damage, debonding was restricted to the skin measured during the experiments.

Table 3 presents the pairs of damaged and undamaged mode shapes for the three damage scenarios. The cells with no numbers are undamaged modes where no pairs were found.

Figs. 15–18 show the damage maps obtained after applying the statistical treatment, and Table 4 presents the performance indicators. It can be observed that the mode shape curvature, GS and the ULS methods failed to detect cases of smaller damage. In addition, the ULS method was affected by the shaker attachment in the case of smaller damage. Only the MSE method was able to correctly detect and locate the damage in the three cases. Furthermore, the MSE method provided, on average, the lowest FPR and FNR.

The GS method was the only algorithm able to detect the smaller damage cases using the numerical model, but the experimental data were unable to detect smaller damage. Perhaps, in the numerical model, the curvatures were more sensitive to small damage than the experimental panel or the experimental measurements did not have the accuracy required by the GS method.

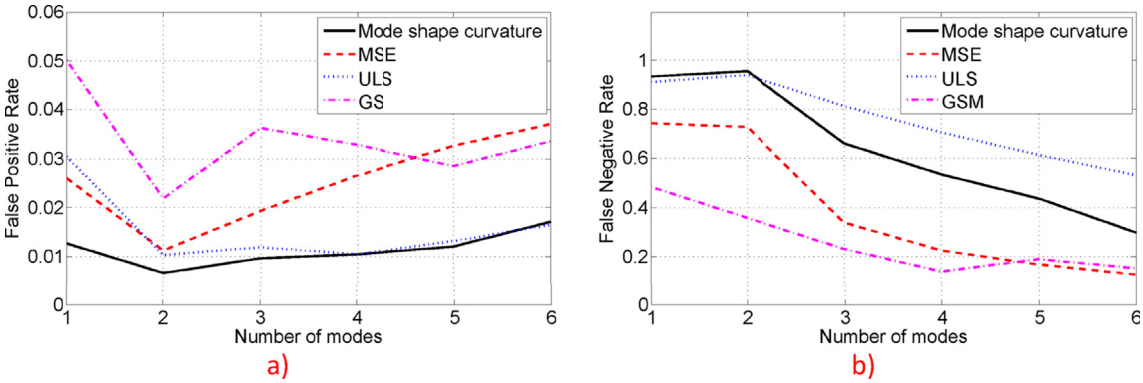


**Fig. 13.** Performance of damage assessment algorithms as a function of number of modes: a) FPR and b) FNR.

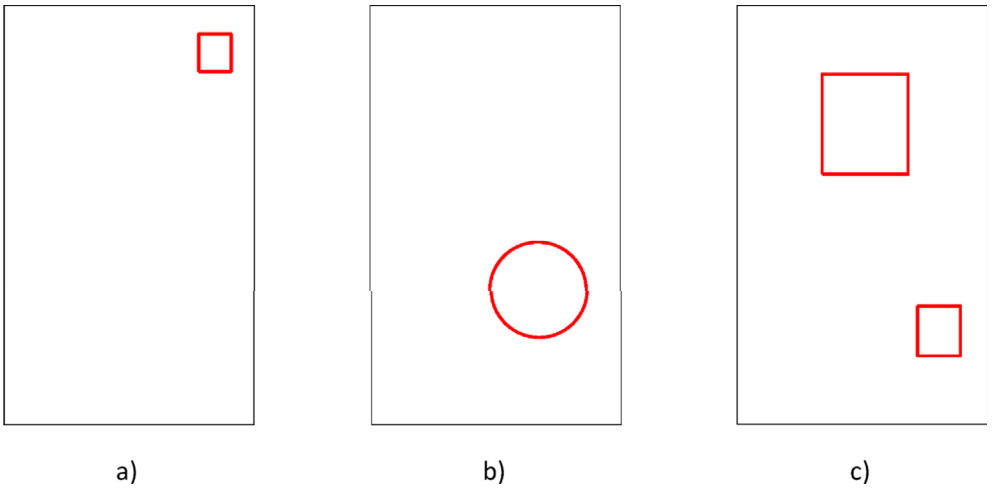


**Fig. 14.** Experimental damage scenarios introduced to panel (red lines indicate debonded regions): a) scenario 1, b) scenario 2 and c) scenario 3. (For interpretation of the references to colour in this figure legend, the reader is referred to the web version of this article.)

**Table 3**
Pairs of damaged and undamaged mode shapes.

| Undamaged | Scenario 1 | | | Scenario 2 | | | Scenario 3 | | |
|---|---|---|---|---|---|---|---|---|---|
| $\omega^U$ (Hz) | $\omega^D$ (Hz) | $\Delta\omega$ (%) | MAC | $\omega^D$ (Hz) | $\Delta\omega$ (%) | MAC | $\omega^D$ (Hz) | $\Delta\omega$ (%) | MAC |
| 444 | 440 | −0.9 | 0.99 | 440 | −0.9 | 0.97 | 425 | −4.3 | 0.98 |
| 481 | 477 | −0.8 | 0.99 | 493 | 2.5 | 0.90 | 483 | 0.4 | 0.60 |
| 801 | 786 | −1.9 | 0.98 | 798 | −0.4 | 0.98 | 807 | 0.7 | 0.99 |
| 985 | 926 | −6.0 | 0.95 | 820 | −16.8 | 0.68 | – | – | – |
| 1214 | – | – | – | – | – | – | – | – | – |
| 1290 | 1289 | −0.1 | 0.92 | 1230 | −4.7 | 0.67 | 1304 | 1.1 | 0.60 |

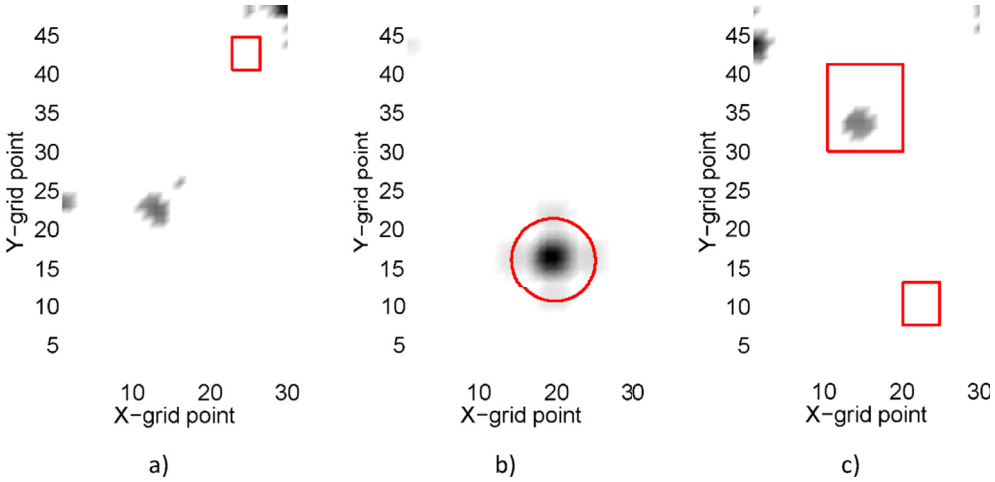


**Fig. 15.** Experimental damage identified by mode shape curvature algorithm: a) case 1, b) case 2 and c) case 3.

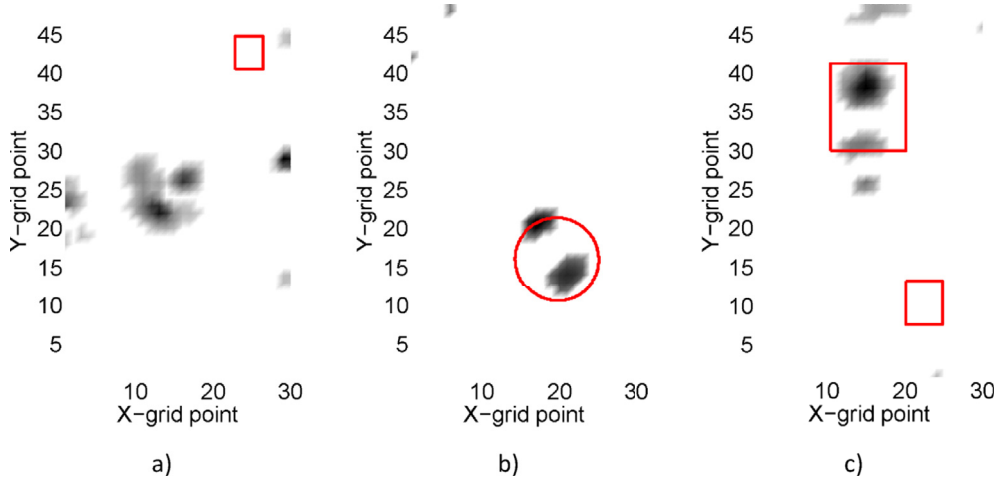


**Fig. 16.** Experimental damage identified by ULS algorithm: a) case 1, b) case 2 and c) case 3.

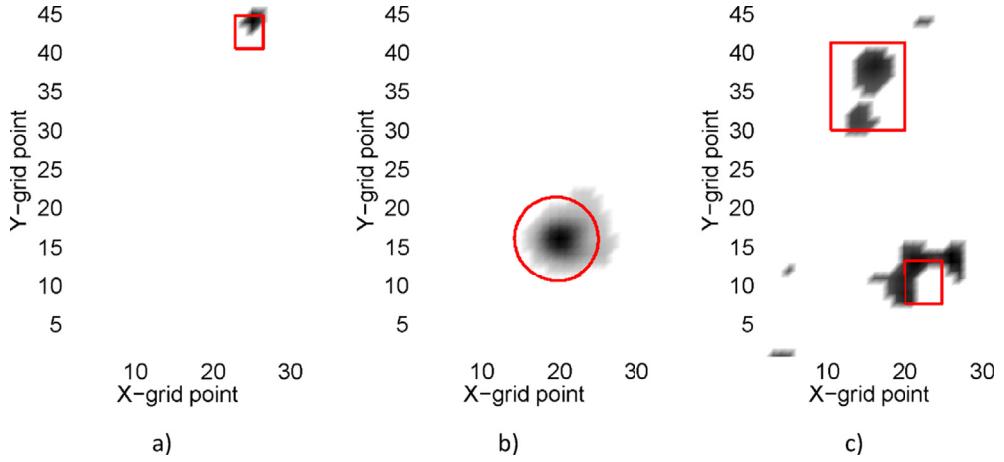


**Fig. 17.** Experimental damage identified by MSE algorithm: a) case 1, b) case 2 and c) case 3.

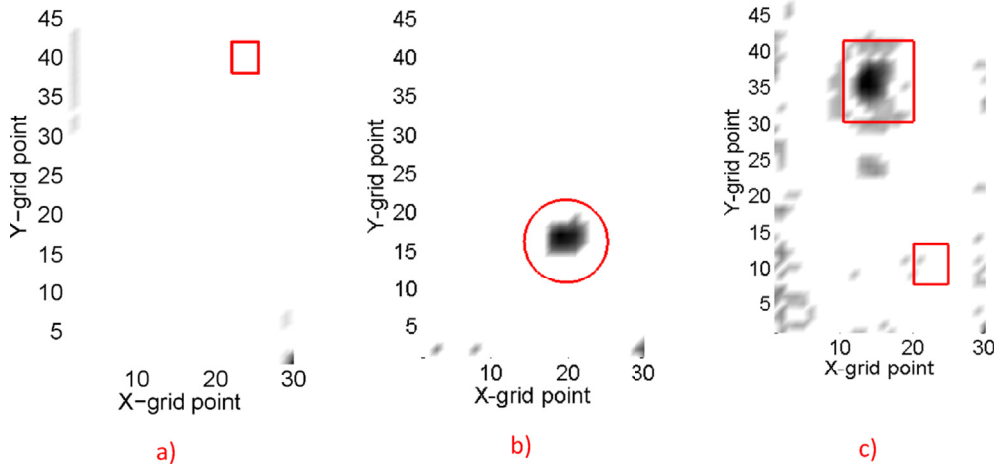


**Fig. 18.** Experimental damage identified by GS algorithm: a) case 1, b) case 2 and c) case 3.

**Table 4**
Performance of damage assessment methodologies with experimental data.

| Method | Case 1 | | Case 2 | | Case 3 | | Average | |
|---|---|---|---|---|---|---|---|---|
| | FPR | FNR | FPR | FNR | FPR | FNR | FPR | FNR |
| Mode shape curvature | 0.019 | 1.000 | 0.030 | 0.177 | 0.010 | 0.649 | 0.020 | 0.609 |
| ULS | 0.070 | 1.000 | 0.007 | 0.684 | 0.023 | 0.774 | 0.033 | 0.819 |
| MSE | 0.001 | 0.750 | 0.021 | 0.190 | 0.033 | 0.583 | 0.018 | 0.508 |
| GS | 0.012 | 1.000 | 0.004 | 0.747 | 0.087 | 0.781 | 0.034 | 0.843 |

## 7. Conclusions

The application of full-field vibration measurements in the assessment of debonding in sandwich structures was investigated. The performance of four methodologies for computing damage indices were evaluated using simulated numerical data. These methodologies were mode shape curvatures, ULS, MSE and GS. Experimental data from an aluminium honeycomb panel in which different damage scenarios were created was acquired by a high-speed 3-D DIC system, and the performance of the four methodologies were evaluated with this data.

The results demonstrated that a high-speed 3-D system can be used to successfully identify debonding in composite panels. Among the four methodologies that were evaluated, the best experimental results were obtained with the MSE method, which was able to correctly detect, locate and roughly quantify damage. The other three methodologies failed to detect smaller damage, and the ULS was affected by the shaker attachment in the case of smaller damage.

However, the MSE method required the damaged and undamaged modes to be paired. This implies that some of the damaged modes with useful information were not used during the damage assessment process because they were not paired with undamaged modes. The GS method, on the other hand, avoids mode-shape pairing. A possible topic of future research is the development of an algorithm that uses MSE in conjunction with the GS method.

## Acknowledgements

The authors acknowledge the financial support of the Chilean National Fund for Scientific and Technological Development (Fondecyt) under Grant No. 1170535 and the Fondequip Program under grant EQM130026.

## References

[1] J.R. Vinson, Sandwich structures: past, present, and future, in: Sandwich Structures 7: Advancing with Sandwich Structures and Materials, 2005. Aalborg, Denmark.
[2] A.S. Herrmann, P.C. Zahlen, I. Zuardy, Sandwich structures technology in commercail aviation: present applications and future trends, in: Sandwich structures 7: Advancing with Sandwich Structures and Materials, 2005. Aalborg, Denmark.
[3] C. Foreman, Nondestructive Detection and Characterization of Damages in Honeycomb Composite Structures, Master Thesis, Iowa State University, 2008.
[4] D. Hsu, Nondestructive evaluation of sandwich structures, in: 8th International Conference on Sandwich Structures, 2008. Porto, Portugal.
[5] H. J, P. D, Evaluation of in-service NDI methods for composite aerospace structures, in: 6th International Workshop NDT in Progress, 2011. Prague.
[6] B. Hayman, Approaches to damage assessment and damage tolerance for FRP sandwich structures, J. Sandw. Struct. Mater. 9 (6) (2007) 571–596.
[7] E. Carden, P. Fanning, Vibration based condition monitoring: a review, Struct. Health Monit. 3 (4) (2004) 355–377.
[8] L. Jiang, K. Liew, M. Lim, S. Low, Vibratory behaviour of delaminated honeycomb structures: a 3-D finite element modelling, Comput. Struct. 55 (5) (1995) 773–788.
[9] V. Burlayenko, T. Sadowski, Dynamic behaviour of sandwich plates containing single/multiple debonding, Comp. Mater. Sci. 50 (4) (2011) 1263–1268.
[10] V.N. Burlayenko, T. Sadowski, Influence of skin/core debonding on free vibration behavior of foam and honeycomb cored sandwich plates, Int. J. Nonlin. Mech. 45 (10) (2010) 959–968.
[11] H.-Y. Kim, W. Hwang, Effect of debonding on natural frequencies and frequency response functions of honeycomb sandwich beams, Compos. Struct. 55 (1) (2002) 51–62.
[12] J. Lou, L. Wu, L. Ma, J. Xiong, B. Wang, Effects of local damage on vibration characteristics of composite pyramidal truss core sandwich structure, Compos. Part B Eng. 62 (2014) 73–87.
[13] A. Shahdin, J. Morlier, Y. Gourinat, Damage monitoring in sandwich beams by modal parameter shifts: a comparative study of burst random and sine dwell vibration testing, J. Sound. Vib. 329 (5) (2010) 566–584.
[14] V. Meruane, V. Del Fierro, A. Ortiz-Bernardin, A maximum entropy approach to assess debonding in honeycomb aluminum plates, Entropy 16 (5) (2014) 2869–2889.
[15] V. Meruane, V. Del Fierro, An inverse parallel genetic algorithm for the identification of skin/core debonding in honeycomb aluminium panels, Struct. Control. Health Monit. 22 (12) (2015) 1426–1439.
[16] P. Cawley, R.D. Adams, The location of defects in structures from measurements of natural frequencies, J. Strain Anal. Eng. Des. 14 (2) (1979) 49–57.
[17] N.A.J. Lieven, D.J. Ewins, Spatial correlation of mode shapes, the coordinate modal assurance criterion (COMAC), in: Proceedings of the Sixth International Modal Analysis Conference, 1988. Orlando, Florida.
[18] A.K. Pandey, M. Biswas, M.M. Samman, Damage detection from changes in curvature mode shapes, J. Sound. Vib. 145 (2) (1991) 321–332.
[19] A.K. Pandey, M. Biswas, Damage detection in structures using changes in flexibility, J. Sound. Vib. 169 (1) (1994) 3–17.
[20] Z. Zhang, A.E. Aktan, Application of modal flexibility and its derivatives in structural identification, Res. Nondestruct. Eval. 10 (1) (1998) 43–61.
[21] Z.Y. Shi, S.S. Law, L.M. Zhang, Structural damage localization from modal strain energy change, J. Sound. Vib. 218 (5) (1998) 825–844.
[22] P. Cornwell, S.W. Doebling, C.R. Farrar, Application of the strain energy damage detection method to plate-like structures, J. Sound. Vib. 224 (2) (1999) 359–374.
[23] Y.Y. Li, L. Cheng, L.H. Yam, W.O. Wong, Identification of damage locations for plate-like structures using damage sensitive indices: strain modal approach, Comput. Struct. 80 (25) (2002) 1881–1894.

[24] D. Wu, S.S. Law, Damage localization in plate structures from uniform load surface curvature, J. Sound. Vib. 276 (1) (2004) 227–244.
[25] D. Wu, S.S. Law, Sensitivity of uniform load surface curvature for damage identification in plate structures, J. Vib. Acoust. 127 (1) (2005) 84–92.
[26] M.K. Yoon, D. Heider, J.W. Gillespie, C.P. Ratcliffe, R.M. Crane, Local damage detection using the two-dimensional gapped smoothing method, J. Sound. Vib. 279 (1) (2005) 119–139.
[27] P. Qiao, K. Lu, W. Lestari, J. Wang, Curvature mode shape-based damage detection in composite laminated plates, Comp. Struct. 80 (3) (2007) 409–428.
[28] P. Moreno-García, H. Lopes, J.A. dos Santos, N.M.M. Maia, Damage localisation in composite laminated plates using higher order spatial derivatives, in, in: Proceedings of the Eleventh International Conference on Computational Structures Technology, 2012. Stirlingshire, UK.
[29] M.N. Helfrick, C. Niezrecki, P. Avitabile, T. Schmidt, 3D digital image correlation methods for full-field vibration measurement, Mech. Syst. Signal Process 25 (3) (2011) 917–927.
[30] W. Wang, J.E. Mottershead, A. Ihle, T. Siebert, H.R. Schubach, Finite element model updating from full-field vibration measurement using digital image correlation, J. Sound. Vib. 330 (8) (2011) 1599–1620.
[31] W. Wang, J.E. Mottershead, T. Siebert, A. Pipino, Frequency response functions of shape features from full-field vibration measurements using digital image correlation, Mech. Syst. Signal Process 28 (2012) 333–347.
[32] F. Trebuña, M. Hagara, Experimental modal analysis performed by high-speed digital image correlation system, Measurement 50 (2014) 78–85.
[33] N.S. Ha, H.M. Vang, N.S. Goo, Modal analysis using digital image correlation technique: an application to artificial wing mimicking Beetle's hind wing, Exp. Mech. 55 (5) (2015) 989–998.
[34] B. Jaishi, W. Ren, Damage detection by finite element model updating using modal flexibility residual, J. Sound. Vib. 290 (1–2) (2006) 369–387.
[35] F. Grubbs, Procedures for detecting outlying observations in samples, Technometrics 11 (1) (1969) 1–21.
[36] X. Dai, F. Yang, Z.S.X. Chen, X. He, Strain field estimation based on digital image correlation and radial basis function, Opt. Lasers Eng. 65 (2015) 64–72.
[37] L.B. Meng, G.C. Jin, X.F. Yao, Application of iteration and finite element smoothing technique for displacement and strain measurement of digital speckle correlation, Opt. Lasers Eng. 45 (1) (2007) 57–63.
[38] J.Q. Zhao, P. Zeng, B. Pan, L.P. Lei, H.F. Du, W.B. He, L. Y, Y.J. Xu, Improved Hermite finite element smoothing method for full-field strain measurement over arbitrary region of interest in digital image correlation, Opt. Lasers Eng. 50 (11) (2012) 1662–1671.
[39] B. Pan, A. Asundi, H. Xie, J. Gao, Digital image correlation using iterative least squares and pointwise least squares for displacement field and strain field measurements, Opt. Lasers Eng. 47 (7) (2009) 865–874.
[40] D. Garcia, Robust smoothing of gridded data in one and higher dimensions with missing values, Comput. Stat. Data Anal. 54 (4) (2010) 1167–1178.
[41] H.L. Weinert, Efficient computation for Whittaker–Henderson smoothing, Comput. Stat. Data Anal. 52 (2) (2007) 959–974.
[42] T. Siebert, T. Becker, K. Spiltthof, I. Neumann, R. Krupka, High-speed digital image correlation: error estimations and applications, Opt. Eng. 46 (5) (2007) 051004.
[43] T. Siebert, R. Wood, K. Splitthof, High speed image correlation for vibration analysis, J. Phys. Conf. Ser. 181 (1) (2009) 012064.
[44] E. Balmes, J.-M.L. Jean-Philippe Bianchi, Structural Dynamics Toolbox User's Guide, Version 6.1, SDTools, 2010.
[45] R.J. Allemang, D.L. Brown, A correlation coefficient for modal vector analysis, in: Proceedings of the First International Modal Analysis Conference, 1982. Orlando, Florida.